



# A Theoretical and Experimental Study of Stress–Strain, Creep and Failure Mechanisms of Intact Coal

Liang Zhang<sup>1,2</sup> · Xiangchun Li<sup>1</sup> · Ting Ren<sup>2,3</sup>

Received: 10 May 2020 / Accepted: 19 August 2020 / Published online: 1 September 2020  
© Springer-Verlag GmbH Austria, part of Springer Nature 2020

## Abstract

Deep mining and drilling activities typically trigger significant deformation of coal/rock roadway and even coal/rock dynamic hazards, which has attracted considerable attention. Hence, in this article, the mechanics and failure properties of intact coal are examined through triaxial compression tests and creep tests. First of all, triaxial compression experiments demonstrated that the complete stress–strain curves of intact coal are characterised by Class-I behaviour; and the post-peak modulus is negative. Second, with increasing confining pressure, peak strength and residual strength rise linearly, whereas elasticity modulus and peak strain increase as a power function form. Thirdly, compared with conventional triaxial load, tiered cyclic load can stiffen the strength of intact coal. Moreover, the data of creep tests are successfully fitted to the Burgers model. Maxwell elasticity modulus is significantly smaller than other creep parameters; Maxwell viscosity coefficient shows a positive correlation with deviatoric stress. Contrarily, Kelvin elasticity modulus and Kelvin viscosity coefficient drop with the rise in deviatoric stress. Additionally, with increasing deviatoric stress, single-step creep strain and average creep strain rate, proposed in this study, increase in a power function form. Finally, failure characteristics of intact coal under triaxial stress could be classified into four types (mainly shear failure and multiple shear fractures). The failure-plane angle generally linearly increases with the rise in confining pressure applied.

**Keywords** Intact coal · Complete stress–strain · Creep · Conventional triaxial load · Tiered cyclic load · Failure mechanisms

## Abbreviations

$B$	The ratio of circumferential strain to axial strain
$c$	Cohesion
$D$	Cylinder diameter
$E$	Elasticity modulus
$E_K$	Kelvin modulus
$E_M$	Maxwell modulus
$k_i$	Post-peak modulus
$L$	Cylinder length
$q$	Axial deviatoric stress

$t$	Time
$\beta$	Failure-plane angle
$\dot{\epsilon}_c$	Average creep rate
$\epsilon_1$	Axial strain
$\epsilon_{\text{creep}}(t)$	Axial strain evaluated a certain time instant $t$
$\epsilon_3$	Circumferential strain
$\epsilon_p$	Peak strain
$\epsilon_c$	Single-step creep strain
$\eta_K$	Kelvin viscosity
$\eta_M$	Maxwell viscosity
$\mu$	Poisson's ratio
$\sigma_n$	Effective normal stress imposed on the failure plane
$\Delta\sigma_s$	Intensity difference
$\sigma_2$	Intermediate principal stress
$\sigma_1$	Major principal stress (axial stress)
$\sigma_3$	Minor principal stress (confining pressure)
$\sigma_p$	Peak strength
$\sigma_r$	Residual strength
$\varphi$	Internal friction angle
CTL	Conventional triaxial load

✉ Xiangchun Li  
chinalixc123@163.com; 108983@cumtb.edu.cn

<sup>1</sup> School of Emergency Management and Safety Engineering, China University of Mining and Technology (Beijing), Beijing 100083, China

<sup>2</sup> School of Civil, Mining and Environmental Engineering, University of Wollongong, Wollongong, NSW 2522, Australia

<sup>3</sup> School of Safety Engineering, China University of Mining and Technology, Xuzhou 221116, Jiangsu, China

SEM	Scanning electron microscope
TCL	Tiered cyclic load
TCS	Triaxial compression strength

## 1 Introduction

In underground mining engineering, the coal/rock mass response to mining-induced stresses and time-dependency may result in significant deformation or even instability failure, posing severe threats to mine operators and infrastructure (Hamza and Stace 2018; Tu et al. 2019). For instance, a pressure burst took place at the Austar Coal Mine, Australia in 2014, causing fatal injuries to two mine workers (Bruce and Jim 2017). A rock burst occurred at the Qianqiu Coal Mine, China in 2011, and resulted in 10 deaths as well as trapping 75 people (Li et al. 2016). An understanding of the changes in geo-mechanical parameters and the failure features of coal has been considered essential for the further development of underground mine design. It will also provide valuable input to the prediction and subsequent control measures for coal/rock dynamic hazards.

In recent decades, scholars have intensively investigated the mechanical features (e.g. complete stress–strain curves) of coal/rock mass from various perspectives. It is widely accepted that contributory factors such as confining pressure ( $\sigma_3$ ), applied stress level, and cyclic loading may strongly affect the mechanics and failure properties of coal. Several studies have shown that according to the differences apparent in the post-peak area, the complete stress–strain curves of rock can be classified into two categories: Class-I and Class-II (Gu et al. 2019; Wawersik and Fairhurst 1970; Zhou et al. 2018). Two post-failure characteristics exhibit a strain rate sensitivity. Wawersik and Fairhurst (1970) declared that Class-II failure behaviour could not be controlled only by stiffening the testing machine because failure would proceed even though the machine stiffness is infinite. Recently, built on the Class-I stress–strain curve, Zhou et al. (2018) tested three types of rocks (marble, black sandstone, and red sandstone) under different stress states and found the strength increased with the rise in  $\sigma_3$ . Moreover, Zhao (2000) intensively reviewed and compared the application of the Mohr–Coulomb and Hoek–Brown strength criteria to the dynamic strength of brittle rock. It is suggested that the Mohr–Coulomb strength criteria can be applied to dynamic triaxial strength in the low  $\sigma_3$  ranges.

Furthermore, coal/rock mass is usually subjected to cyclic and even dynamic stress during vibration from blasting, drilling, or adjacent coal seam mining. Thus, it is of considerable significance to study the impacts of cyclic loads on the mechanical behaviours of coal. Fuenkajorn and Phueakphum (2010) evaluated the effect of cyclic loading on the elasticity, compression strength, and time dependency of salt

rock. The experiments demonstrated that the visco-plastic parameters calculated from the cyclic loading test are less than those under static loading. Recently, Jiang et al. (2017) also explored the impact of cyclic stress on gas-containing coal in terms of acoustic emission (AE) characteristics, seepage, and energy dissipation, but the time-dependent behaviour and destructive features of coal were not addressed.

During deep mining, creep of discontinuities is a part of the fundamental properties for coal and rocks, which is prone to contribute to the large deformation of coal/rock roadway, or even coal bump or rockburst (Bruce and Jim 2017; Cai et al. 2019; Jia et al. 2018; Zhan et al. 2020). Delay failure may take place several days or years after excavation. In rock mechanics and rock engineering, for instance, Nicolas et al. (2017) investigated the brittle and semi-brittle creep of Tavel limestone deformed at ambient temperature, and they stated that deformation and failure type depends on  $\sigma_3$ . Soon afterwards, Hamza and Stace (2018) conducted creep tests on intact and fractured muddy siltstone under confinement ( $\sigma_3 = 0\text{--}6$  MPa). Regression analysis revealed that the Burgers model is suitable to predict the creep behaviour. Indeed, the deformability strongly depends on the stress level applied and the time allowed for the coal or rocks to creep. Sone and Zoback (2013) studied the ductile creep behaviour, elastic modulus, and brittle strength of shale-gas reservoir rocks. They demonstrated that visco-plastic creep strain is roughly linear with the imposed deviatoric stress. Subsequently, Rassouli and Zoback (2018) carried out the comparison of short-term (4-h) and long-term (4-week) creep tests in clay- and carbonate-rich shale samples in a time-cyclical manner. The experimental results revealed that regardless of the applied stress history, the shale samples creep following a single trend through time, and the power law can estimate this relation. In mining engineering, for example, based on the short-term and creep tests on coal samples, Yang et al. (2015) put forward a nonlinear damage model. Additionally, Sun et al. (2019) investigated the stability of a typical coal roadway and revealed its rheological property. More recently, Zhan et al. (2020) analysed the instability mechanism of a soft-rock coal roadway with a buried depth of 1336 m. They noted that the convergence trend of omnidirectional, rheological, and large deformation is the main feature for the in-depth roadway simultaneously accompanied by a ‘domino effect’. In general, numerous meaningful numerical and qualitative relationships to interpret the rheological feature of coal or rocks were obtained through these publications. The fracture mechanics of coal, however, were neglected; in particular, the failure mechanism of coal during compression and creep processes.

Investigating the failure mechanism of coal is vital for the safety of mining activities. In the rock mechanics field, Jaeger et al. (2007) systematically summarised the failure mode of rocks with uniaxial/triaxial compressive and uniaxial

tensile stress. Ma and Haimson (2016) examined the failure properties of two porous sandstones subjected to true triaxial stresses. Their experiments revealed the energetic influence of the intermediate principal stress ( $\sigma_2$ ) on the failure of porous sandstone, whereas true triaxial stress tests are hard to achieve in the ordinary laboratory. Afterwards, Mansouri and Ajalloeian (2018) observed the macroscopic morphology and microscopic features of salt specimens after failure under uniaxial compression and creep trials. They deemed that grain boundary cracking and grain boundary sliding are the dominant deformation mechanisms. Simultaneously, Zhao et al. (2018) discovered that the failure-plane angle ( $\beta$ ) of Jinping marble samples change almost linearly with changing  $\sigma_2$ . In terms of the mining field, Tu et al. (2019) compared tectonic and intact coal specimens under compression and evaluated the role of tectonic coal in coal and gas burst. Yang et al. (2020b) recently analysed the average particle ejection velocity of coal burst depending on the fragments of coal specimens under uniaxial stress. Moreover, it is widely accepted that coal is a kind of complicated and porous material containing numerous randomly distributed flaws and pores in different scales (Gu et al. 2019). The type and pressure of the gas may impact the mechanical features (Li et al. 2019; Xie et al. 2017; Zhang et al. 2019a). Viète and Ranjith (2006) showed that uniaxial compression strength and elastic modulus ( $E$ ) of brown coal decreased due to the absorption of  $\text{CO}_2$ , with no evident triaxial compression strength (TCS) or  $E$  decrease in the triaxial experiments. Subsequently, Masoudian et al. (2014) suggested that 72 h ( $\text{CO}_2$  injection time) is a reasonable time to permit the influence of  $\text{CO}_2$  to develop (for the coal sample of the size  $25 \times 50$  mm). However, failure properties, especially the failure-plane angle  $\beta$  of coal, have been neglected in recent documents (Masoudian et al. 2014; Tu et al. 2019; Zhang et al. 2019b).

Although extensive research has been conducted on mechanical and failure features of the rocks, minimal investigations exist which simultaneously deal with the stress–strain, creep, and failure characteristics, especially  $\beta$ , for intact coal under various  $\sigma_3$  and loading paths. Therefore,

this paper focuses on the mechanical properties (e.g. brittle strength, peak strain, and elasticity modulus), creep, and failure mechanisms (e.g. post-peak modulus, failure patterns, and  $\beta$ ) of intact coal under different  $\sigma_3$  and triaxial loading paths (conventional triaxial load and tiered cyclic load). Unless otherwise specified, tiered cyclic load (TCL), in this paper, represents both the load in the tiered cyclic compression and tiered cyclic creep trials. Similarly, the same is genuine for the conventional triaxial load (CTL). The findings will provide a framework to assess the geomechanics and failure mechanisms of coal mass and are of great significance for mine engineering design and the prevention and control of coal/rock dynamic hazards.

## 2 Experimental

### 2.1 Material

The coal material (see Fig. 1) used in the present work was collected from the third coal seam of Yuwu Coal Mine, located south of Shanxi province, China. The basic physical parameters of the coal material are as follows: volatile matter content  $V_{\text{daf}} = 11.74\%$ , moisture content  $M_{\text{ad}} = 1.15\%$ , ash content  $A_{\text{ad}} = 5.25\%$ , as well as fixed carbon content  $\text{FC}_{\text{ad}} = 82.61\%$ . It signifies that the tested material belongs to lean coal (a kind of bituminous coal).

In rock mechanics and rock engineering, it is recognised that the initial geometry of the pre-existing bedding planes or bedding dip angles has substantial impacts on the fracture mechanics concerning rocks (Berčáková et al. 2020; Ding et al. 2020; Li et al. 2020; Pan and Lü 2018; Shen et al. 2020; Wang et al. 2016; Yang et al. 2020a; Zhou et al. 2017). Coal, as one of the sedimentary rocks, however, has an extremely complex internal structure (Kong et al. 2019). The micromorphology inside coal material used in this study was examined using scanning electron microscope (SEM) technology. As detailed in Fig. 2, the general observation of micrographs shows the anisotropy of coal. The random appearances of geometrical structures, such as weak shear



**Fig. 1** Necessary information on experimental material: **a** one of the original coal blocks sourced from the coal mine; **b** coal blocks after being cored; **c** standard intact coal samples without macroscopic bedding planes

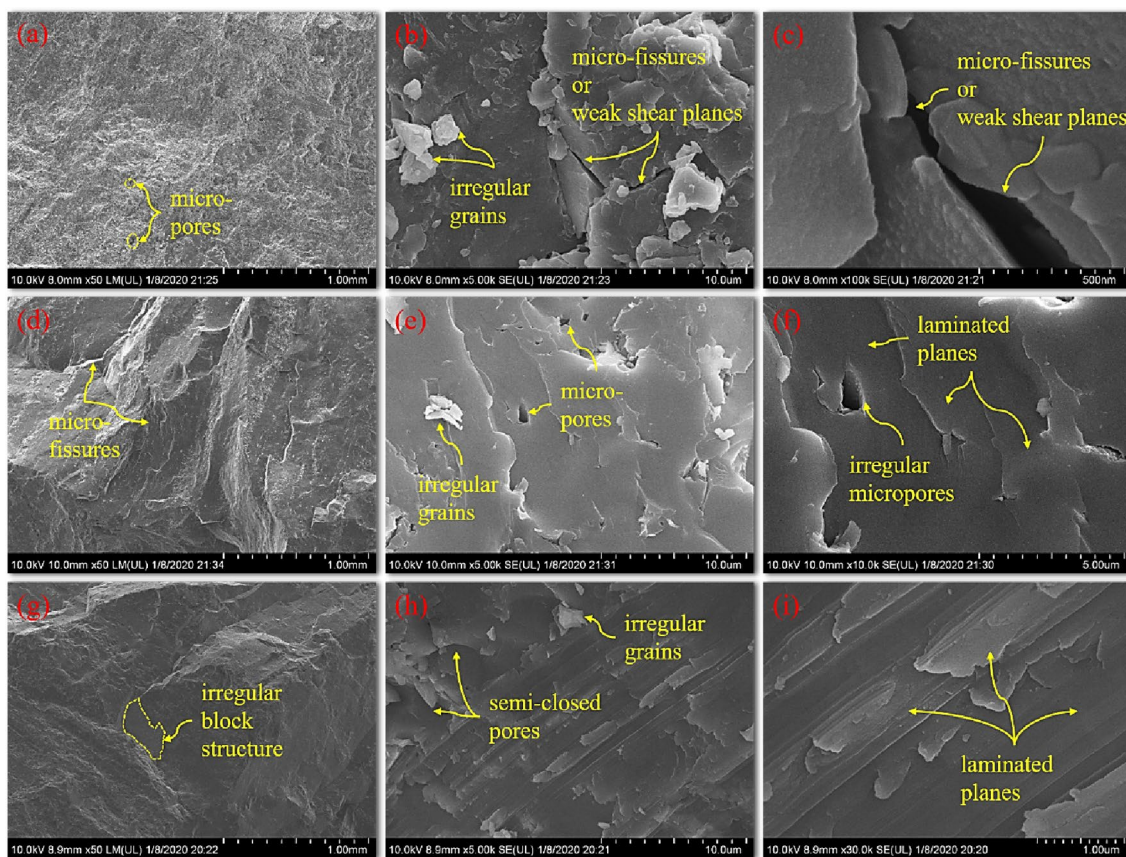


**Fig. 2** Micrographs of three randomly selected observation zones within original coal material. Zone1: **a** micropores appear in the general observations (SEM 50 times); **b** weak shear planes (or shear cracks) and irregular grains are the main features (SEM 5,000 times); **c** shear planes of weakness with various intersection angles (SEM 100,000 times). Zone2: **d** microfissures are observed (SEM 50 times);

**e** irregular grains and micropores are obvious (SEM 5000 times); **f** partial area is characterised by laminated planes and irregular micropores (SEM 10,000 times). Zone3: **g** the overall morphology is uneven (SEM 50 times); **h** semi-closed pores and irregular grains are identifiable (SEM 5000 times); **i** this zone is characterised by anisotropy, e.g. irregular laminated planes (SEM 30,000 times)

planes, irregular micropores, and irregular grains, are the main features (yellow arrows in Fig. 2). Hence, for the sake of minimising the effect of bedding planes and bedding dip angles, we cored along the perpendicular orientation of intact coal blocks (Tu et al. 2019).

Furthermore, cores, 50 mm in diameter, were carefully drilled from similar coal blocks in the laboratory to reduce any variability in mechanical properties. Cylindrical specimens (Fig. 1c) were trimmed to a length-to-diameter ( $L/D$ ) ratio of 2 following the procedures outlined by the International Society for Rock Mechanics (ISRM) (Hamza and Stace 2018). Lastly, the coal samples were dried at 105°C for 24 h to eliminate the influence of humidity.

## 2.2 Equipment

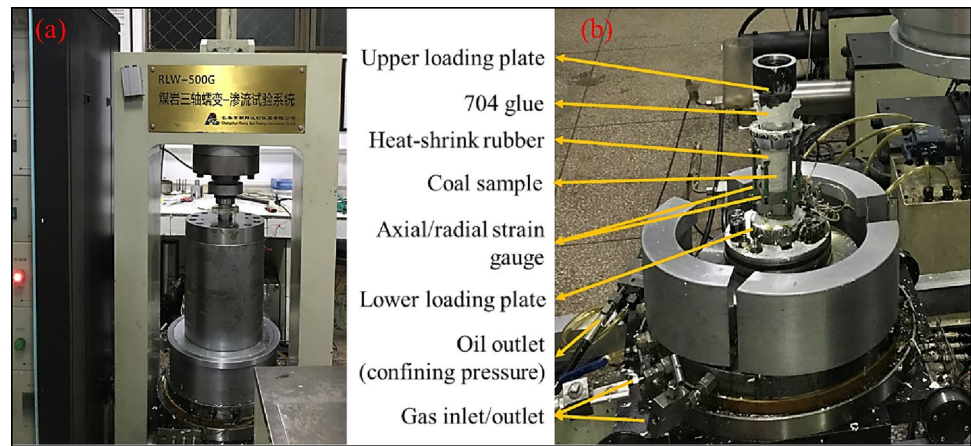
The majority of mechanical tests, in the present study, were carried out employing the ‘RLW-500G coal/rock triaxial creep-seepage experimental system’ (Wang et al. 2019), as

shown in Fig. 3. The maximum axial load and maximum lateral pressure ( $\sigma_3$ ) are 500 kN and 50 MPa, respectively. The experimental data, for example, stress–strain, gas pressure, gas seepage, and acoustic emission (AE), can be recorded directly through the data acquisition system.

## 2.3 Methods

The primary purpose of this work was to investigate the complete stress–strain, creep, failure mechanisms of gas-containing intact coal under different  $\sigma_3$  and loading paths (including CTL and TCL simultaneously). Initially, four-set triaxial compressive tests (i.e.  $\sigma_3 = 2, 4, 6, 8$  MPa) were conducted to examine the influence of  $\sigma_3$  on the stress–strain and failure features of gas-bearing ( $N_2$ ) intact coal. The axial stress was imposed at a rate of 30 N/s during the experiments. Following on, the compression experiment using  $CO_2$  was performed on the coal sample (YW0111) subjected to the same pressures ( $\sigma_3 = 2$  MPa,  $p_1 = 1$  MPa). Then, the tiered

**Fig. 3** RLW-500G electrohydraulic servo-controlled coal/rock mechanics testing system and assembled coal specimen: **a** RLW-500G testing system; **b** an assembled coal sample (two layers of heat-shrink rubber on the sample outside to prevent gas leakage)



cyclic compression test was carried out under the same conditions ( $\sigma_3 = 2$  MPa,  $p_1 = 1$  MPa). It was noticed that tiered cyclic compression is a particular method of cyclic loading that the axial stress amplitude increases monotonously from one cycle to the next cycle (Jiang et al. 2017). In the tiered cyclic compression tests, the rate of loading and unloading was also held constant (30 N/s).

In most events, the previous Refs. (Hou et al. 2019; Rassouli and Zoback 2018; Yang et al. 2015; Zhang et al. 2019a) mainly adopted either conventional multistage creep or tiered cyclic creep to examine the creep behaviour or damage changes of coal/rock. In the current paper, those two methods were employed simultaneously to explore the time-dependent behaviour of intact coal (bearing gas) under the same circumstances ( $\sigma_3 = 2$  MPa,  $p_1 = 1$  MPa). The maximum axial stress applied to the coal specimen increased from one cycle to the next cycle, while  $\sigma_3$  was kept constant in the tiered cyclic creep test. According to the triaxial compression results of the sample subjected to  $\sigma_3 = 2$  MPa, the deviatoric stress ( $q = \sigma_1 - \sigma_3$ ) was applied stepwise within the range from 40 to 90% of TCS until failure occurred. The experiments were performed at ambient temperature ( $26 \pm 2$  °C). A total of eight out of ten samples

were successfully measured. The specific experimental procedures are shown in Table 1.

### 3 Results

#### 3.1 Complete Stress–Strain Curves

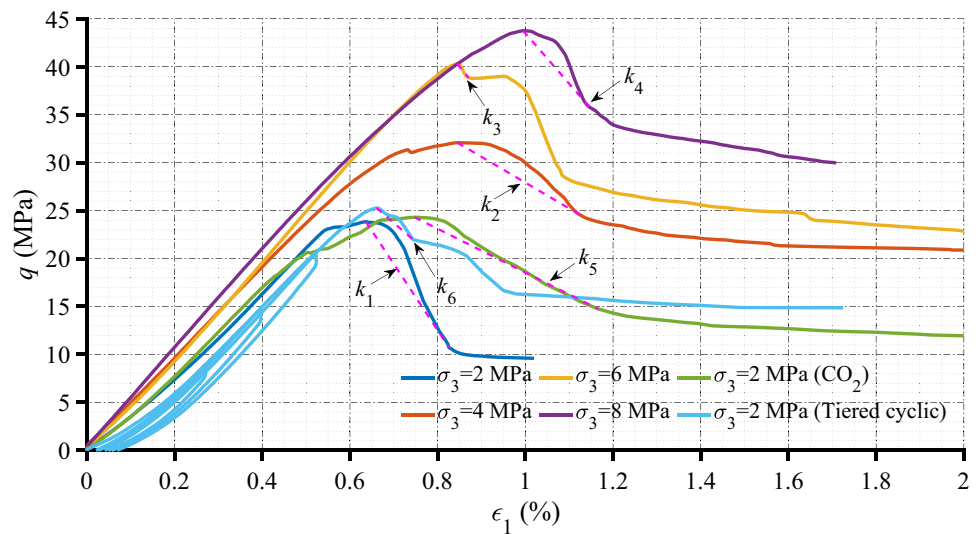
It is generally accepted that the complete stress–strain curves of rocks under conventional compression can be divided into five segments: (1) viscoelastic deformation (pore and fissure closure); (2) quasi-linear elastic deformation; (3) crack growth and damage accumulation (yield stage); (4) post-peak softening; (5) residual strength (Alkan et al. 2007; Pepe et al. 2018; Yang et al. 2015). As illustrated in Fig. 4, regardless of loading paths and  $\sigma_3$ , intact coal experienced the above deformation stages in the compressive experiments. Overall, TCS increases with the rise in  $\sigma_3$ . When  $\sigma_3$  is 2, 4, and 8 MPa, TCS for samples YW012, YW013, and YW014 is 23.84, 32.08, and 43.75 MPa, respectively. TCS for sample YW013 is over 34.56% higher than that of sample YW012, whereas lower than that of sample YW014.

**Table 1** Geometric information of coal samples and the experimental projects

Sample no	L (mm)	D (mm)	Test type	$\sigma_3$ (MPa)
YW012	99.66	49.20	Conventional triaxial compression	2
YW013	99.80	49.10		4
YW015	99.30	49.94		6
YW014	99.22	49.50		8
YW0111	99.02	49.20		2
YW019	99.10	49.00	Tiered cyclic compression	2
YW01101	100.00	49.22	Conventional multistage creep	2
YW0112	99.80	49.12	Tiered cyclic creep	2

CO<sub>2</sub> (99.99%) was used in the test of sample YW0111, and N<sub>2</sub> (99.99%) in other trials. Gas pressure was maintained in all trials ( $p_1 = 1$  MPa). Moreover, samples with unsaturated adsorbed gas were adopted in all experiments, which could examine the coupling relation between gas seepage and deformation of the coal matrix

**Fig. 4** Stress–strain relation of intact coal specimens under triaxial compression tests



Secondly, it seems that tiered cyclic compression can enhance the strength of an intact coal sample. As shown in Fig. 4, TCS of sample YW019 is 25.28 MPa, greater than that for sample YW012 (23.84 MPa). Also, a the gas with strong adsorption capacity ( $\text{CO}_2$ ) was utilised in the compression test on sample YW0111. From Fig. 4, it can be seen that the TCS for sample YW0111 is 24.30 MPa, marginally higher than that of sample YW012. The peak strain of sample YW0111 (0.747%) is also greater than that of sample YW012 (0.636%).

In most cases, the intact coal samples show the Class-I failure properties in terms of the complete stress–strain curves. It is characterised by ‘stable’ fracture propagation and retains some strength even after the peak strength has been exceeded; this failure can be controlled. In contrast to this ‘stable’ fracture development, the destruction of Class-II is self-sustaining. The elastic energy stored in the coal interior when the applied stress equals the peak strength is

enough to maintain fracture development until the coal has lost all virtual strength. In this case, the failure cannot be arrested unless the strain energy is removed.

Moreover, the post-peak modulus ( $k_i$ ) referring to the slope of the line from the peak strength point to the initiation point of the residual strength (Zhou et al. 2018) is introduced here. The Class-I curve is characterised by negative  $k_i$ , while the Class-II curve is characterised by a positive  $k_i$ . As schematically indicated in Fig. 4, the post-peak modulus of all coal sample is negative ( $k_i < 0$ ,  $i = 1-6$ ). The axial strain of each coal sample increases monotonously in the post-peak area, and strain softening emerges until the coal reaches the residual deformation area.

### 3.2 Creep Curves

Comparison of Figs. 5 and 6 shows that regardless of conventional multistage creep or tiered cyclic creep, the

**Fig. 5** Conventional multistage creep curve for the coal sample YW01101

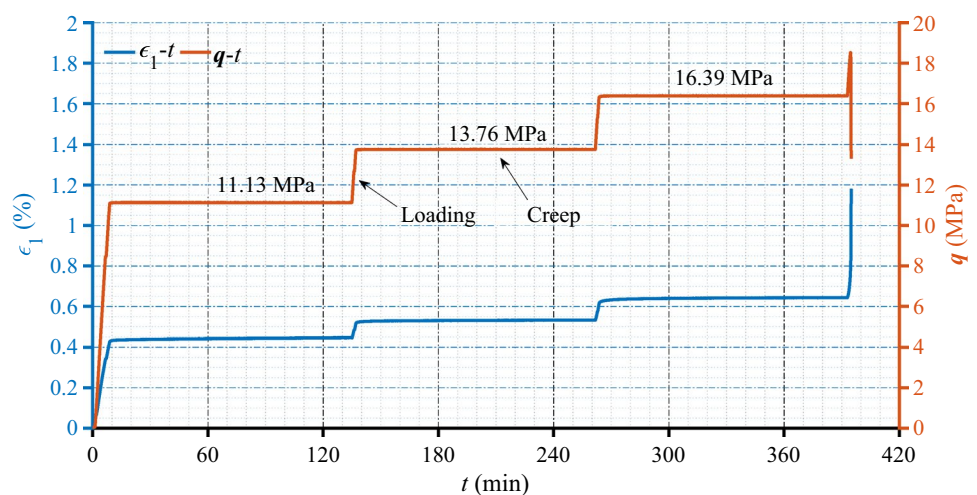
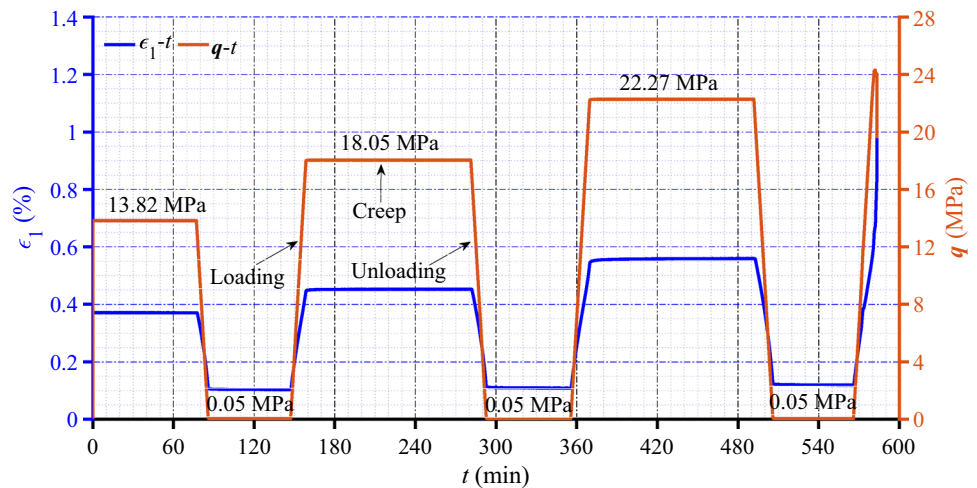


**Fig. 6** Tiered cyclic creep curve for the coal sample YW0112



deformability of intact coal depends significantly on the applied deviatoric stress ( $q$ ). From Fig. 5, we can observe that the axial strain of sample YW01101, owing to the loads at the previous three stable creep stages, increases firstly from 0.4% to 0.5%, and then goes up to 0.6%, and eventually rises sharply to 1.1% until failure occurs with the gradual enlargement of  $q$ . Meanwhile, the stress level of  $q$  at the first three creep stages is 11.13, 13.76, and 16.39 MPa, respectively, which approximately accounts for 46.7, 57.7, and 68.8% of the TCS of the sample YW012. The brittle fracture takes place as soon as  $q$  moves up to 18.52 MPa in the last stage; subsequently,  $q$  rapidly drops to below 14 MPa (see Fig. 5). The peak strength (18.52 MPa) of sample YW01101 appearing in the last loading stage is close to 77.7% of the TCS (23.84 MPa) for sample YW012.

Furthermore, compared with conventional multistage creep, that of tiered cyclic creep turns out to be more significant in terms of peak strength. As shown in Fig. 6, the peak strength of sample YW0112 is 24.29 MPa, over 31% greater than that of sample YW01101. This finding is in line with the result in the triaxial compression tests where TCS of sample YW019 is higher than that of sample YW012. It is evident that compared with the CTL, TCL can stiffen the strength of intact coal samples based on the observations in the compression tests and creep tests.

In addition, Fig. 6 indicates that although  $q$  was unloaded, axial strain in the previous three unloading phases increased from one cycle to the next cycle. The corresponding axial strain is approximately 0.10, 0.11, and 0.12%, respectively. A possible explanation for this might be that although the elastic strain energy is released in the unloading stage, the dissipated energy in the coal interior is cumulative. Then, due to energy accumulation and energy dissipation, the damage is continually amassed (Jiang et al. 2017). Meanwhile, microcrack propagation and visco-plastic deformation occur, which triggers the increment of axial strain stepwise.

## 4 Discussion

### 4.1 Peak Strength, Residual Strength, and Intensity Difference

Mechanical parameters such as peak strength ( $\sigma_p$ ), residual strength ( $\sigma_r$ ), elastic modulus ( $E$ ), and peak strain ( $\epsilon_p$ ) play an essential role in the stability evaluation of coal. As discussed in Sect. 3.1,  $\sigma_p$  and  $\sigma_r$  of coal are strongly dependent on  $q$  and the loading path, which is in general agreement with prior works of Ref. (Heap et al. 2009; Rassouli and Zoback 2018). It should be noticed that both the peak strength and residual strength refer to the axial stress rather than the deviatoric stress ( $q$ ). Here, we put forward the intensity difference ( $\Delta\sigma_s$ ) defined as the difference in  $\sigma_p$  and  $\sigma_r$ , i.e.

$$\Delta\sigma_s = \sigma_p - \sigma_r. \quad (1)$$

From Fig. 4, on the basis of elastoplastic mechanics, the mechanical parameters can be calculated, as represented in Table 2. Comparing Fig. 4 and Table 2 shows that  $\sigma_p$  and  $\sigma_r$  of sample YW019 are higher than those of sample YW012. This finding shows an agreement with the analysis that TCL can improve the strength of intact coal, as discussed in Sects. 3.1 and 3.2. Additionally, the mechanical parameters  $\sigma_p$ ,  $\sigma_r$ ,  $E$ , and  $\epsilon_p$  from sample YW0111 are also more significant than those from sample YW012. It is anticipated that the absorption of  $\text{CO}_2$  may change the elastic modulus or even the strength of the coal sample (Li et al. 2019; Masoudian et al. 2014; Viete and Ranjith 2006). However, in the current paper, a coal specimen with unsaturated adsorption gas was used; thus, no systematic investigation was performed to handle this information. It is suggested that in future work, allowing the coal to adsorb gas for as long as maybe 72 h and then measuring the coal deformation and gas permeability under different

**Table 2** Mechanical parameters of coal under the triaxial compression regime

Sample no	$\sigma_p$ (MPa)	$\sigma_r$ (MPa)	$\Delta\sigma_s$ (MPa)	$E$ (GPa)	$\varepsilon_p$ (%)	$\sigma_3$ (MPa)
YW012	25.84	11.60	14.24	4.394	0.636	2
YW013	36.08	25.11	10.97	4.805	0.845	4
YW015	46.31	27.32	18.99	5.296	0.844	6
YW014	51.75	38.03	13.72	5.062	0.995	8
YW0111	26.30	13.80	12.50	4.675	0.747	2
YW019	27.28	16.87	10.41	–	0.661	2

confinements would be beneficial to assess the influence of  $\text{CO}_2$  on the mechanics of coal.

As mentioned previously, the main aim of this work was to examine the effects of  $\sigma_3$  and loading paths (CTL and TCL) on the stress–strain, creep, and failure features of intact coal. Therefore, along with the test data (excluding sample YW019 and YW0111), we will evaluate the impact of  $\sigma_3$  on the mechanical parameters (including  $\sigma_p$ ,  $\sigma_r$ ,  $\Delta\sigma_s$ ,  $E$ , and  $\varepsilon_p$ ) in Sect. 4.1 and 4.2 in turn.

The Mohr–Coulomb strength criterion is well established and widely used in geotechnical engineering application, such as rock engineering modelling and design (Si et al. 2019; Zhao 2000). The initial concept of the Mohr–Coulomb strength criterion signifies that the shear strength of rocks comprises two parts: a constant cohesion and friction varying with normal stress. According to the Mohr hypothesis, destruction emerges on a critically oriented plane when the shear stress on this plane reaches the shear strength which can be expressed as:

$$\tau = c + \sigma_n \tan \varphi, \quad (2)$$

where  $\tau$  is the shear strength,  $\sigma_n$  is the effective normal stress acting on the fracture plane, as well as  $c$  and  $\varphi$  which is the cohesion and internal friction angle of rock material, respectively. The Mohr–Coulomb strength criterion was elaborated

upon by Zhao (2000). The orientation of the failure critical plane can be deduced by

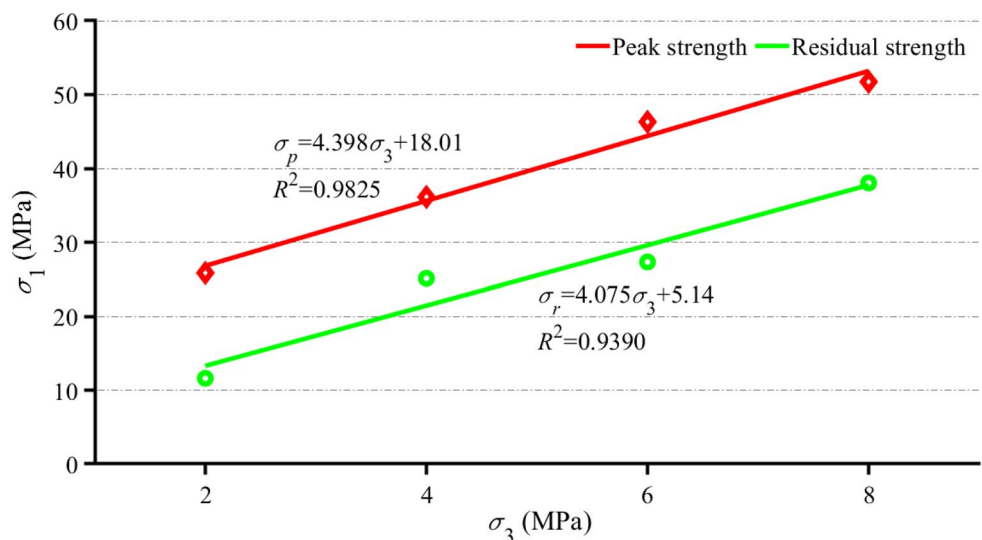
$$\beta = \frac{\pi}{4} + \frac{\varphi}{2}, \quad (3)$$

where  $\beta$  is the intersection angle of the direction between the minor principal stress ( $\sigma_3$ ) and the shear plane (also known as the failure-plane angle). In terms of effective principle stresses (Ma et al. 2013; Renani and Martin 2020), the Mohr–Coulomb strength criterion can also be given by:

$$\sigma_1 = \frac{2c \cos \varphi}{1 - \sin \varphi} + \sigma_3 \frac{1 + \sin \varphi}{1 - \sin \varphi}. \quad (4)$$

It can be perceived from Eqs. (2) and (4) that the Mohr–Coulomb criterion may predict a linear relationship between axial stress and  $\sigma_3$  at failure.

In the light of the Mohr–Coulomb criterion, we validate the relationship between the coal strength ( $\sigma_p$  and  $\sigma_r$ ) and  $\sigma_3$  using the experimental data of conventional triaxial compression (excluding sample of YW0111 and YW019). As plotted in Fig. 7, both the  $\sigma_p$  and  $\sigma_r$  for coal overall linearly increase with the rise in  $\sigma_3$ . This relationship can be expressed by:

**Fig. 7** Linear fitting results of  $\sigma_p$  and  $\sigma_r$  of intact coal under different  $\sigma_3$ 



$$\sigma_p = 4.398\sigma_3 + 18.01 \tag{5}$$

and

$$\sigma_r = 4.075\sigma_3 + 5.14, \tag{6}$$

respectively. Good regression coefficients of  $R^2=0.9825$  and  $0.9390$  are calculated for  $\sigma_p$  and  $\sigma_r$ , respectively.

Then, the internal friction angle can be determined by combining Eqs. (4) and (5), i.e.  $\varphi = 39^\circ$ . Although  $\varphi$  calculated by this method has been usually a constant value (Zhou et al. 2018), it is reasonable to estimate  $\sigma_p$  and  $\sigma_r$  of intact coal using the Mohr–Coulomb criterion. This finding is broadly in good agreement with the previous study (Yang et al. 2015). In addition, the rupture angle of coal can be calculated, i.e.  $\beta = 64^\circ$ , which will be further discussed in Sect. 4.5.

Moreover, the stress in the post-peak area drops drastically. Thus, the concept of the intensity difference ( $\Delta\sigma_s$ ) is proposed here. Comparing Figs. 7 and 8 shows that although  $\sigma_p$  and  $\sigma_r$  exhibit a linear relationship with  $\sigma_3$ ,  $\Delta\sigma_s$  seems to have no dependence on  $\sigma_3$ .

### 4.2 Elastic Modulus and Peak Strain

The elastic modulus ( $E$ ) is one of the vital mechanical parameters reflecting the coal deformation characteristics. The  $E$  for coal under triaxial stress state can be calculated by (Zhang et al. 2019b):

$$E = \frac{\sigma_1 - 2\mu\sigma_3}{\epsilon_1}, \tag{7}$$

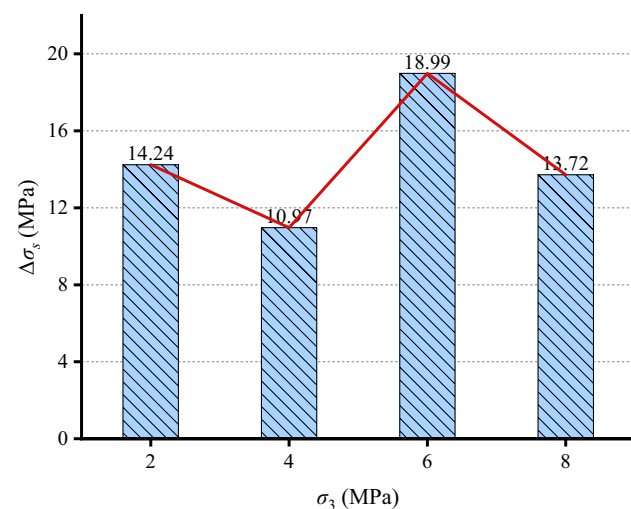


Fig. 8  $\Delta\sigma_s$  versus  $\sigma_3$  for conventional triaxial compression tests

$$\mu = \frac{B\sigma_1 - \sigma_3}{\sigma_3(2B - 1) - \sigma_1}, \tag{8}$$

$$B = \frac{\epsilon_3}{\epsilon_1}, \tag{9}$$

where  $\mu$  is Poisson’s ratio under the triaxial stress state;  $\epsilon_3$  is the circumferential strain;  $B$  represents the ratio of circumferential strain to axial strain. Because  $E$  and  $\mu$  are constant at the linear elastic deformation stage, we can figure out the  $E$  for coal samples calculating the slope of the line ranging from 40 to 50% of TCS in Fig. 4. And  $E$  for coal samples under conventional triaxial stress (excluding sample YW019) is presented in Table 2. It shows that with increasing  $\sigma_3$ ,  $E$  also increases nonlinearly, from 4.394 to 5.062 GPa.

Yang et al. (2012) stated that the power function could describe the influence of  $\sigma_3$  on  $E$  for red sandstone. As exhibited in Fig. 9, thus, the power function is also employed to depict the relationship between  $E$  of intact coal and  $\sigma_3$  (except for the sample YW0111 and YW019). According to the nonlinear regression analysis, we can obtain the equation as follows:

$$E = 4.09\sigma_3^{0.1187}, \tag{10}$$

with a reasonable goodness of fit ( $R^2=0.8025$ ).

Additionally, recent studies (Yang et al. 2015; Yin et al. 2015) seem to neglect the effect of  $\sigma_3$  on the peak strain ( $\epsilon_p$ ) of intact coal (bearing gas). Figure 9 shows that with increasing  $\sigma_3$ ,  $\epsilon_p$  also increases in a power function form:

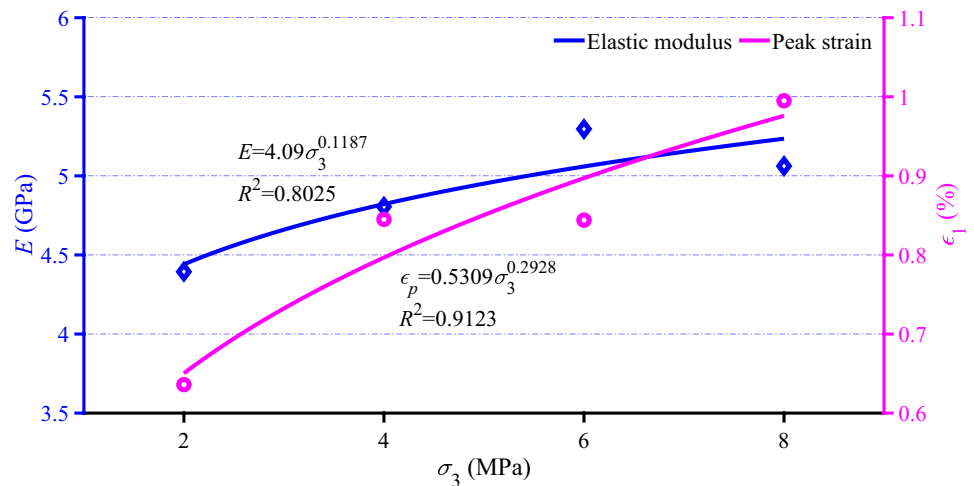
$$\epsilon_p = 0.5309\sigma_3^{0.2928}, \tag{11}$$

with a good regression coefficient of  $R^2=0.9123$ .

### 4.3 Creep Strain and Strain Rate

The deformation of coal is sensitive to stress (e.g. uniaxial or triaxial compression) and time (such as creep and relaxation). In general, the idealised creep curve usually exhibits four principal phases: (1) instantaneous elastic strain because of instantaneous load; (2) transient creep with sharp strain increments, but at a decelerated strain rate; (3) secondary creep at low, or near-constant strain rate; (4) possible accelerated creep with rapid strain increment until failure occurs, which would cost more given the extended time conducting laboratory experiments (Hamza and Stace 2018). It is almost unrealistic to achieve the ideal tertiary (or accelerated) creep through prejudging the deviatoric stress ( $q$ ) and the time given for the coal to creep. Throughout the experimental program, as depicted in Figs. 5 and 6, the coal samples did not experience the ideal tertiary creep within

**Fig. 9** Power fitting curves of  $E$  and peak strain  $\epsilon_p$  of intact coal under different  $\sigma_3$



the timescale. Therefore, the accelerated creep is out of the scope of this paper.

To recognise the accuracy of creep deformation during the conventional triaxial creep test and tiered cyclic creep test, we redraw the typical creep curves in Figs. 10 and 11, respectively. It should be pointed out that the strain–time curves are adjusted to zero intercepts. In most cases, when an instantaneous deviatoric load is imposed on the coal, the axial strain shows a jump, e.g. the AB stage in Fig. 10. When the imposed deviatoric stress  $q$  is held constant, the primary creep appears at a decelerating strain rate, i.e. BC segment, where point B is the initiating point of creep. With the extension of time, the secondary creep (steady-state creep) would be apparent (CF curve). If the time allowed is long enough, the coal may gradually transition from steady-state creep to tertiary creep (accelerated creep). Because of the restriction of the laboratory conditions, there is not any accelerated creep in a limited time domain. From Figs. 5 and 6, we can

observe that  $q$  rises sharply to the maximum value first and then drops abruptly during the final loading process, indicating the appearance of the failure. As shown in Fig. 11, the creep is triggered at the point J, where the load is kept constant. During the unloading process (e.g. at NP segment in Fig. 11), there is no noticeable creep due to the low-stress level (the axial stress and confining pressure is just 2.05 MPa and 2 MPa, respectively). Additionally, from Fig. 6 it can be seen that even though the axial stress is held constant (2.05 MPa) at the first three unloading stages, the axial strain (with respect to the NP line in Fig. 11) is 0.10, 0.11, and 0.12%, respectively, which shows a gradually increasing trend. It is reasonable to assume that the previous load may contribute to the plastic deformation and accumulative damage.

This paper promotes single-step creep strain ( $\epsilon_c$ ) which refers to the strain difference between the end point of secondary creep and the initiating point of transient creep,

**Fig. 10** Typical curve of conventional triaxial creep, taking the specimen YW01101 under deviatoric stress ( $q = 13.76$  MPa) as an example

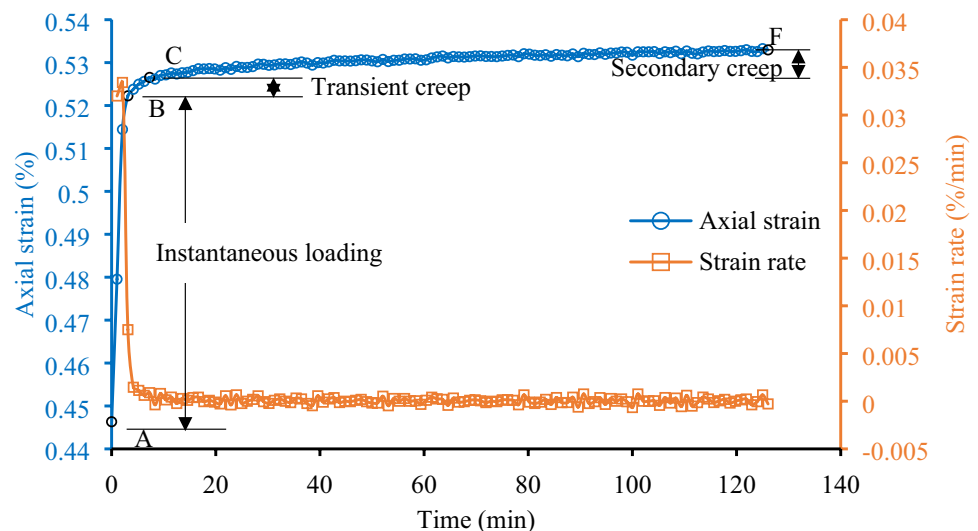


**Fig. 11** Typical curve of tiered cyclic creep, considering the specimen YW0112 at the second cycle as an example

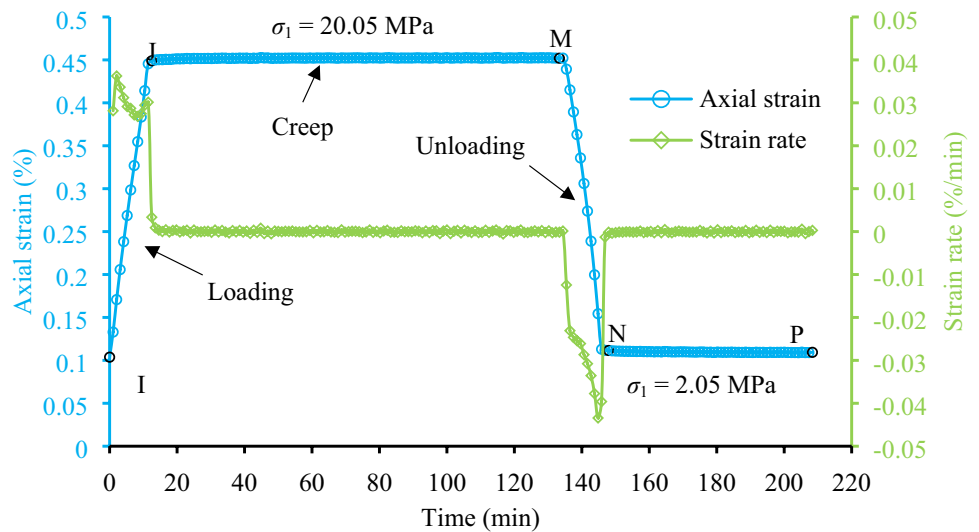


**Table 3** Single-step creep strain  $\epsilon_c$  and average creep rate  $\dot{\epsilon}_c$  for samples YW01101 and YW0112

	YW01101			YW0112 <sup>a</sup>	
	Stage1	Stage2	Stage3	Cycle2 load	Cycle3 load
$q$ (MPa)	11.13	13.76	16.39	18.05	22.27
$\epsilon_c$ (%)	0.013	0.015	0.021	0.004	0.012
$\dot{\epsilon}_c$ (%/min)	1.047e-04	1.196e-04	1.726e-04	3.354e-05	9.644e-05

<sup>a</sup>Creep data of the first 53 min corresponding to the IM line in Fig. 11 is missing due to a minor mechanical fault. The single-step creep strain in the first cycle cannot be estimated accurately. But it does not affect the analyses of the remaining steps in the tiered cyclic creep test, because the secondary creep curves undergo similar stages as detailed in Fig. 11. Hence, we concentrate on the analyses of the second and third cycle for the tiered cyclic creep on sample YW0112 here

for instance, the strain difference between points F and B (Fig. 10), or points M and J (Fig. 11). Similarly, in the present study, the average creep rate ( $\dot{\epsilon}_c$ ), defined as the arithmetic average of creep strain rate (including the whole process of transient creep and secondary creep), is introduced, e.g. the average creep rate of the BF curve in Fig. 10 is  $1.196 \times 10^{-4}$ %/min. According to the experimental data, we can calculate  $\epsilon_c$  and  $\dot{\epsilon}_c$ , as presented in Table 3.

The results in Table 3 demonstrate that  $\epsilon_c$  and  $\dot{\epsilon}_c$  depend highly on both the time and stress applied to the coal samples. Overall, more significant stress or sufficient time intervals may trigger more considerable  $\epsilon_c$  and  $\dot{\epsilon}_c$ . This finding is in line with previous studies (Hamza and Stace 2018; Jia et al. 2018). In addition, Hamza and Stace (2018) found a power-law function can best express the relationship between the secondary creep strain rate and  $q$  for the fractured siltstone. Based on the creep data sourced from sample YW01101, the power function is employed here to fit the relationship between  $\epsilon_c$  and  $q$ :

$$\epsilon_c = 5.358 \times 10^{-4} q^{1.302}, \tag{12}$$

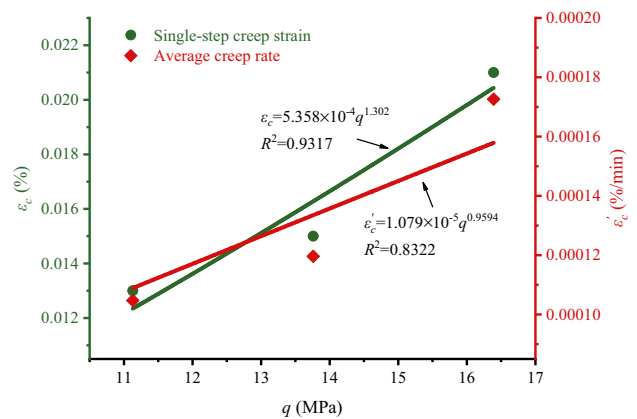


**Fig. 12** Power fitting results of single-step creep strain  $\epsilon_c$  and average creep rate  $\dot{\epsilon}_c$  for sample YW01101 with the rise in deviatoric stress  $q$

with a good regression correlation ( $R^2 = 0.9317$ ). From Fig. 12 it can be seen that  $\dot{\epsilon}_c$  also increases by rising a  $q$  value; this relation can be described by the following equation ( $R^2 = 0.8322$ ):

$$\dot{\epsilon}_c = 1.079 \times 10^{-5} q^{0.9594}. \quad (13)$$

#### 4.4 Analysis of Creep Model

The secondary creep stage is vital for the stability of rock engineering projects. Creep experimental data for coal/rock are frequently examined and fitted employing the best rheologic equations or mechanical models. Burgers model is one of the most common constitutive laws which has been widely applied to model creep behaviours of coal/rock (Hamza and Stace 2018; Mansouri and Ajalloeian 2018; Yang et al. 2015; Zhang et al. 2019a). This model is a form of connection in series by Kelvin body and Maxwell body. Burgers model possesses instantaneous deformation properties, the transient creep, and secondary creep. The constitutive equation for this model in a three-dimensional stress state can be written as (Hamza and Stace 2018):

$$\epsilon_{\text{creep}}(t) = \frac{\sigma_1 - \sigma_3}{E_M} + \frac{\sigma_1 - \sigma_3}{\eta_M} t + \frac{\sigma_1 - \sigma_3}{E_K} \left( 1 - \exp\left(-\frac{E_K}{\eta_K} t\right) \right), \quad (14)$$

where  $\epsilon_{\text{creep}}(t)$  is the axial strain measured at a certain time instant  $t$ ,  $E_K$  and  $\eta_K$  are Kelvin's elasticity modulus and viscosity coefficient, respectively, and  $E_M$  and  $\eta_M$  are Maxwell's elasticity modulus and viscosity coefficient, respectively.

In this paper, these creep parameters were calculated, as detailed in Table 4, through the least-squares regression method employing Matlab (Mathworks). The parameters in Table 4 represent the best value for forecasting the creep behaviour of each intact coal sample. The initial definition of the Boltzmann overlapping principle reveals that the creep strain triggered by the stress imposed on the sample at a specific moment in the past was equal to the sum of the strain derived from the different stresses at that moment. The prevision of the testing results employing the Burgers model can be plotted in Figs. 13 and 14 (black lines represent the simulation curves). The fitted results demonstrated that the Burgers model is appropriate to predict the transient creep and secondary creep of intact coal.

Furthermore, as can be seen from Table 4, Burgers model parameters are prone to be affected by the deviatoric stress  $q$  and loading path. In the Burgers model, the Maxwell unit exhibits the characteristic of steady-state creep (the creep simulated by the Maxwell model is non-recoverable), whereas the Kelvin body illustrates the feature of transient creep, which can be immediately recovered upon the removal of the stress field (Hamza and Stace 2018). Maxwell elasticity modulus ( $E_M$ ) determines the instantaneous elastic strain in the secondary creep, and as shown in Table 4, it is much smaller than other creep parameters. The Maxwell viscosity coefficient ( $\eta_M$ ) can reflect the variation of the strain rate of the secondary creep. It is the highest among of all creep parameters and increases with the rise in  $q$ . Such a trend shows that steady-state creep is singularly dependent on  $q$ , as illustrated in Figs. 13 and 14, and the coal sample deformed noticeably under a high  $q$ .

Compared with Maxwell parameters, Kelvin's elasticity modulus ( $E_K$ ) and viscosity coefficient ( $\eta_K$ ) decrease considerably by increasing  $q$  (except for stage1 for specimen YW01101) and show a high-stress dependence. As listed in Table 4, it signifies that the Kelvin element behaves with an extremely high modulus and very high resistance to viscous flow (Mansouri and Ajalloeian 2018). By increasing  $q$  step by step, both elastic deformation and viscous flow (as depicted in Figs. 13 and 14) become exaggerative, triggering reduced  $E_K$  and  $\eta_K$ . Generally, for all tested specimens,  $\eta_M$  is a great deal larger than  $\eta_K$ , and it is ten times to a hundred times higher than  $\eta_K$ . However,  $E_M$  is much smaller than  $E_K$ ; in fact, it is just a few hundredths of  $E_K$ . Further investigation of these creep parameters for a broader range of  $\sigma_3$  and  $q$  may be performed in future work.

#### 4.5 Failure Patterns and Failure-Plane Angle of Coal

In rock mechanics, several failure patterns are known depending upon the lithology, microstructure and configuration of stress imposed (Masoudian et al. 2014; Mcbeck et al. 2020). Jaeger et al. (2007) systematically summarised rock failures at various uniaxial/triaxial compressive and uniaxial tensile stresses. However, the fracture surfaces of the coal materials, especially their

**Table 4** Creep parameters of intact coal samples YW01101 and YW0112

	$\sigma_1 - \sigma_3$ (MPa)	$E_M$ (GPa)	$\eta_M$ (GPa min)	$E_K$ (GPa)	$\eta_K$ (GPa min)	$R^2$
YW01101						
Stage1	11.13	0.026	156.960	2.376	18.502	0.995
Stage2	13.76	0.027	344.172	1.391	4.682	0.968
Stage3	16.39	0.026	350.139	1.050	6.921	0.981
YW0112						
Cycle2 load	18.05	0.040	4301.716	4.652	19.821	0.856
Cycle3 load	22.27	0.041	971.217	2.376	13.025	0.964

**Fig. 13** Prediction of the experimental data of conventional triaxial creep (for sample YW01101) using the Burgers model

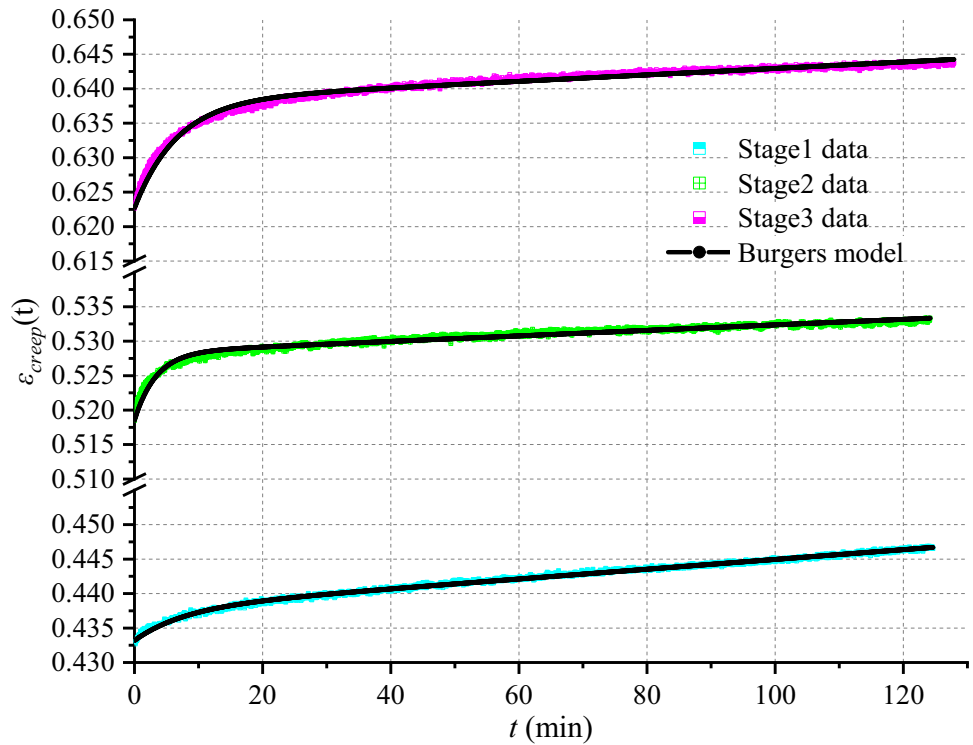
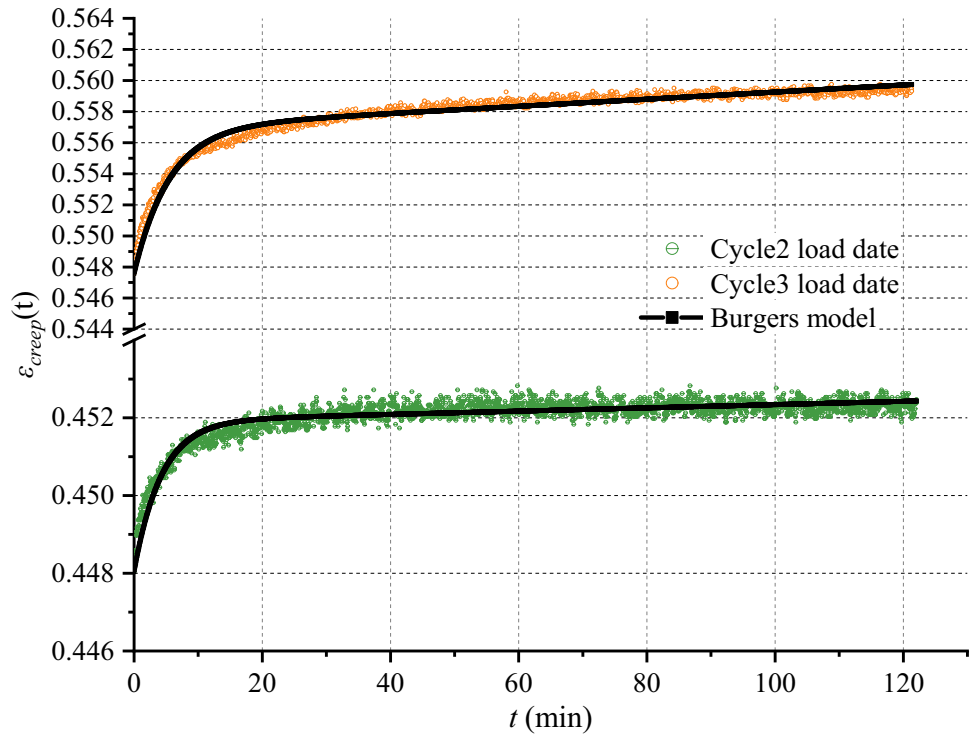


**Fig. 14** Prediction of the experimental data of tiered cyclic creep (for specimen YW0112 at load period) employing the Burgers model



failure-plane angle  $\beta$  (the intersection angle between the shear failure surface and minimum principal stress) are neglected in recent works of Ref. (Masoudian et al. 2014; Tu et al. 2019; Wang et al. 2019; Xu et al. 2020; Zhang et al. 2019b).

Coal fails when the surrounding stress exceeds the tensile, compressive, or shear strengths of the coal formation, whichever is reached first. This can be identified in Fig. 15 (a greyscale image) with the fracture surfaces and  $\beta$  of coal samples after triaxially compressed and crept. Furthermore,

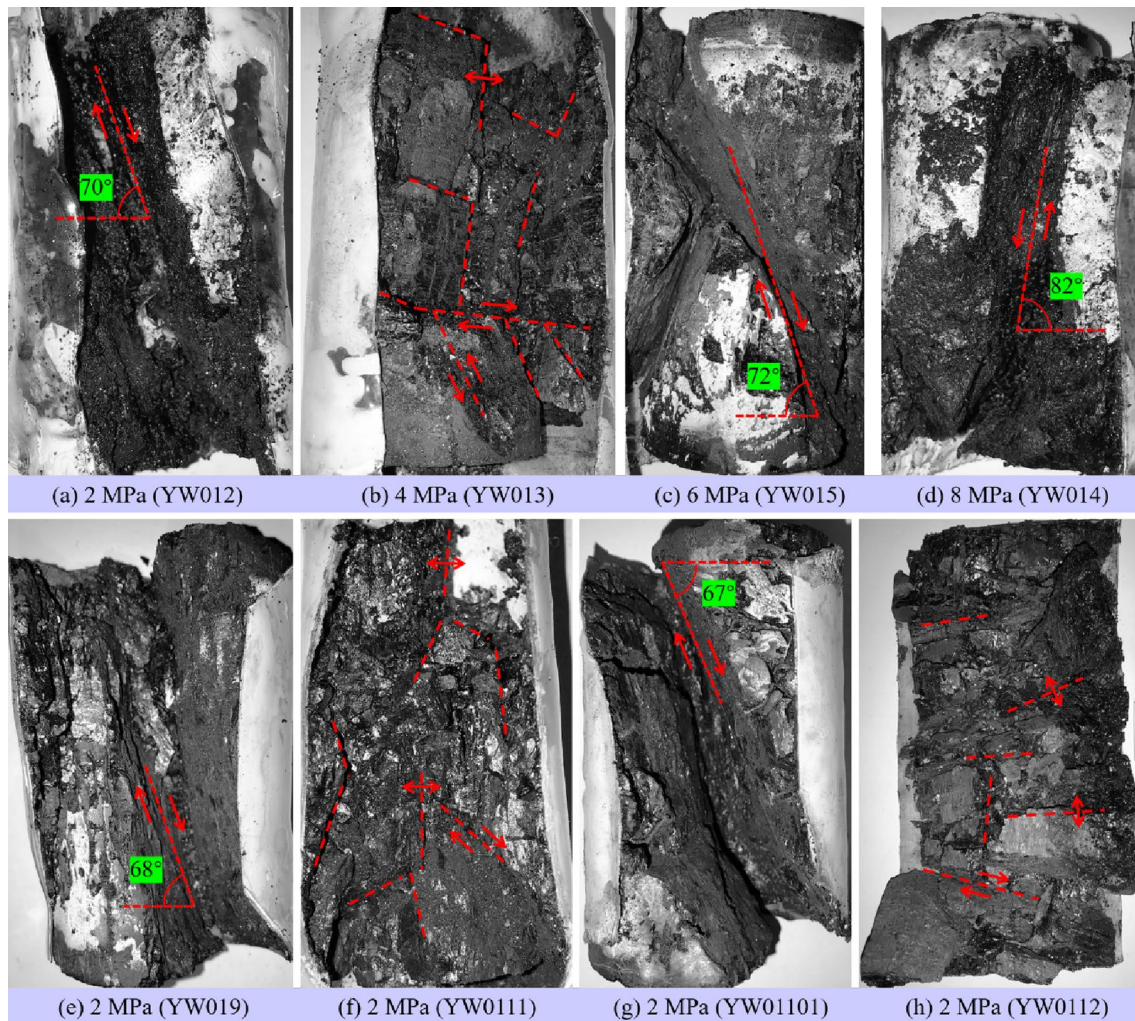


**Fig. 15** The fracture morphology (greyscale image) of the intact coal under different  $\sigma_3$ : **a–d** conventional triaxial compression; **e** conventional triaxial compression using  $\text{CO}_2$ ; **f** tiered cyclic compression; **g** tiered cyclic creep; **h** conventional multistage creep

the failure of coal can be classified into four mechanisms, as illustrated in Fig. 16. At low  $\sigma_3$ , the combination of longitudinal splitting and shear may occur (Fig. 16a). With a moderate amount of  $\sigma_3$ , longitudinal fracturing is suppressed, and failure appears along a single defined plane of fracture (Fig. 16b). This shear plane is generally inclined at an angle less than  $45^\circ$  from the axial stress direction and the plane is characterised by shear displacement along its surface and known as a shear fracture, which is one of the most common types of failure. In some cases, failure takes place along two conjugate shear planes located symmetrically with respect to the axial direction and is referred to as a Y-shaped shear fracture (Fig. 16c). Under some circumstances, if coal becomes sufficiently ductile with the rise in  $\sigma_3$ , a network of small shear fractures (multiple parallels and conjugate failure planes) occurs, accompanied by plastic deformation of the individual coal grains (Fig. 16d). In this case, many triangular or wing-shaped microcracks will emerge inside

the coal (Fig. 15b, f and h). The multiple shear fracture is also one of the most common patterns of failure. In a word, with the moderate or relatively high  $\sigma_3$ , the failure pattern of coal is mainly shear fracture and multiple shear fractures.

The development of the failure plane(s) accompanies the fracture process in coal. The experimental results demonstrate that the  $\beta$  of intact coal is significantly impacted by  $\sigma_3$ . Regardless of the conventional triaxial compression test and tiered cyclic creep test ( $\sigma_3 = 2$  MPa), the  $\beta$  for coal samples (Fig. 15a, e and g) is almost unchanged ( $67\text{--}70^\circ$ ), which is close to the value calculated in Sect. 4.1 based on the Mohr–Coulomb criterion. Beyond that, the variation of  $\beta$  with  $\sigma_3$  is considerably strong, increasing from about  $72^\circ$  ( $\sigma_3 = 6$  MPa) to  $82^\circ$  ( $\sigma_3 = 8$  MPa). It is evident that the increase in  $\sigma_3$  would elicit greater  $\beta$ . As shown in Fig. 17, this trend can be approximated by a linear relationship with a good regression coefficient ( $R^2 = 0.8296$ ). This finding is consistent with the experimental results of sandstone

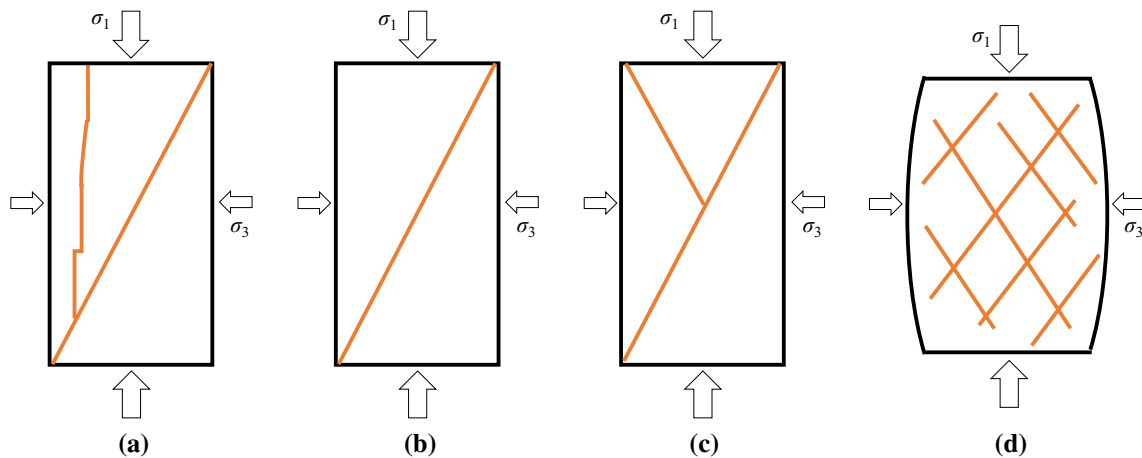


**Fig. 16** Four failure patterns for intact coal under triaxial stresses: **a** combination of longitudinal splitting and shear; **b** shear fracture (single shear plane); **c** Y-shaped shear failure; **d** multiple shear fractures

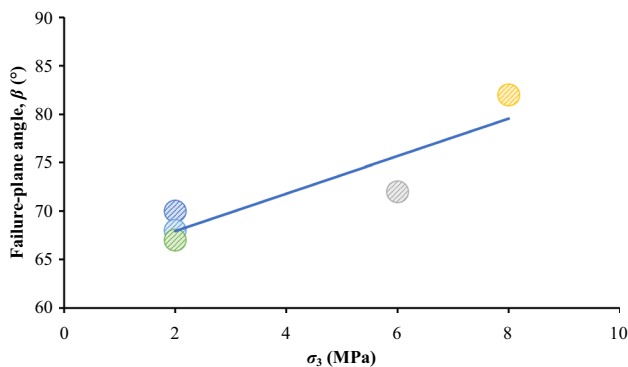


**Fig. 17** Relationship between failure-plane angle  $\beta$  and  $\sigma_3$ . The data points were linearly simulated

reported in recent studies (Ma and Haimson 2016; Zhou et al. 2018).

This paper presents the results of testing and modelling of intact coal. Coal is an anisotropic and heterogeneous material (Barbosa et al. 2020). The existence of macroscopic discontinuities may weaken the strength of coal seams or rock masses (Jiang et al. 2019). As mentioned in Sect. 2.1, the weak shear planes (microfissures) and micropores inside coal were observed using SEM technology. The coal discontinuity and heterogeneity may somewhat limit these findings; nevertheless, it has crucial implications for the geo-mechanical modelling and safety production of coal mines.

Moreover, in deep mining, the elastic strain energy released violently and suddenly from coal or coal measure rocks is prone to trigger coal burst or rockburst, especially in geological structural zones, such as a fold, bedding fault, and cutting fault (Cai et al. 2019; Tu et al. 2019). Since coal burst is highly related to coal failure processes, it is very significant to focus on the mechanical properties and

failure behaviours of coal and other coal measure rocks. Furthermore, during underground longwall mining, the vertical stress concentrates on the front of the coal face owing to the removal of solid coal. When the abutment stress exceeds the coal strength, the coal fails, and elastic strain energy will release, which may potentially contribute to a coal burst. Therefore, prior identification of the stress concentration zone and such burst-potential regions, and ongoing investigative studies into prediction and control measures are vital to minimise the risk of injury or disruption (Bruce and Jim 2017).

## 5 Conclusions

The primary purpose of this paper was to understand the complete stress–strain, creep, and failure mechanisms of intact coal under different  $\sigma_3$  and loading paths (including CTL and TCL simultaneously). The operations mainly consisted of four series of tests (listed in Table 1) where  $\sigma_3$  was held constant in each project (between 2 and 8 MPa).

Regardless of conventional triaxial compression or tiered cyclic compression, all intact coal samples show Class-I failure features in terms of the complete stress–strain curves; and the post-peak modulus is negative ( $k_i < 0$ ,  $i = 1-6$ ). It is characterised by ‘stable’ fracture propagation and retains some strength even after the stress level exceeded peak strength, which signifies this destruction is controllable. The failure model seems to transition from brittle to quasi-brittle with increasing  $\sigma_3$  gradually.

Within the tested scale of stresses, the conventional triaxial compression experiments have revealed the critical influence of  $\sigma_3$  on deformation behaviours and the failure properties of coal. The peak strength and residual strength of coal linearly increase with the rise in  $\sigma_3$  (2–8 MPa). This

relation can be well predicted via the linear Mohr–Coulomb criterion (as expressed by Eqs. 5 and 6, respectively). But the intensity difference introduced in the current study appears to be independent of  $\sigma_3$ . Moreover, with increasing  $\sigma_3$ , the elastic modulus and peak strain are identified to rise in a power function form (Eqs. 10 and 11, respectively).

Compared with CTL, TCL would enhance the strength (both in compression and creep experiments) of intact coal under the same circumstances ( $\sigma_3 = 2$  MPa,  $p_1 = 1$  MPa). A possible explanation for this might be that the deviatoric stress  $q$  plays a vital part in closing up the shear bands or consolidating the compaction bands, which will stiffen up the intact coal samples in the end. In addition, the steady-state strain in the previous three unloading stages increases stepwise, which may result from the cumulative dissipated energy in the coal interior in the tiered cyclic creep test.

Moreover, the data of creep tests were successfully fitted to the Burgers model, exhibiting elasto-viscoplastic characteristics. It revealed that  $E_M$  is far less than that of other creep parameters. However,  $\eta_M$ , much larger than other creep parameters, can reflect the variation of the strain rate of the secondary creep, and linearly increases with the rise in  $q$ . On the contrary, by increasing  $q$ , both elastic deformation and viscous flow become exaggerative, leading to the reduction of  $E_K$  and  $\eta_K$ . Beyond that, the single-step creep strain and the average creep rate, proposed in this paper, show an increasing trend in the power function laws (Eqs. 12 and 13, respectively) with the rise in  $q$ .

Finally, the experimental results of triaxial compression and creep demonstrated that the failure modes of intact coal under triaxial stress can be classified into four types in total: the combination of longitudinal splitting and shear; shear fracture (single shear plane); Y-shaped shear failure; multiple shear fractures. Furthermore, the quantitative analysis of the failure-plane angle  $\beta$  shows that it is positively correlated to  $\sigma_3$ .

In the end, the contributing factors, such as the rank of coal due to the metamorphism, the range of stress level applied to the coal, and the timescale applied to the investigation of creep for coal might somewhat limit the findings. Therefore, future work may be conducted using different types of coal to study its mechanical features, however, with a broader range of  $\sigma_3$  and  $q$ , as well as enough time given to the coal to creep. Nevertheless, these findings in the present paper provide a theoretical framework for future studies to assess the geomechanics and failure mechanisms of intact coal. It also has a valuable application in areas such as the geo-mechanical modelling of mines' stability, roadway support, and the mitigation of coal/rock dynamic hazards.

**Acknowledgements** This work was supported by the Natural Science Foundation of Beijing Municipality (Grant No. 8192036); the National Key Research and Development Program of China (Grant

No. 2018YFC0808301); the Youth Foundation of Social Science and Humanity, Ministry of Education of China (Grant No. 19YJCZH087); the State Key Laboratory Cultivation Base for Gas Geology and Gas Control (Henan Polytechnic University) (Grant No. WS2018B04); and the Fundamental Research Foundation for the Central Universities (Grant No. 2009QZ09). The authors also acknowledge Prof. Jianping Wei, Mr Xiaolong Chen, and Mr Suye Jia for their support during the experimental process. Additionally, the first author would like to express sincere appreciation for the scholarship provided by the China Scholarship Council (CSC No. 201906430024) and University of Wollongong. The authors are grateful for the anonymous reviewers' insightful comments and thank Mr Kevin Marston for proof-reading the manuscript.

## Compliance with Ethical Standards

**Conflict of Interest** The authors declare that there is no conflict of interest.

## References

- Alkan H, Cinar Y, Pusch G (2007) Rock salt dilatancy boundary from combined acoustic emission and triaxial compression tests. *Int J Rock Mech Min Sci* 44:108–119. <https://doi.org/10.1016/j.ijrmm.2006.05.003>
- Barbosa K, Esterle J, Chen ZW (2020) Scaling compressive strength from mini-cylinder specimens of sub-bituminous coal. *Rock Mech Rock Eng* 53:2839–2853. <https://doi.org/10.1007/s00603-020-02083-6>
- Berčáková A, Melichar R, Souček K (2020) Mechanical properties and failure patterns of migmatized gneiss with metamorphic foliation under UCS test. *Rock Mech Rock Eng* 53:2007–2013. <https://doi.org/10.1007/s00603-019-02012-2>
- Bruce H, Jim G (2017) A review of the geomechanics aspects of a double fatality coal burst at Austar Colliery in NSW, Australia in April 2014. *Int J Min Sci Technol* 27:3–7. <https://doi.org/10.1016/j.ijmst.2016.10.002>
- Cai W, Dou LM, Si GY, Cao AY, Gong SY, Wang GF, Yuan SS (2019) A new seismic-based strain energy methodology for coal burst forecasting in underground coal mines. *Int J Rock Mech Min Sci* 123:104086. <https://doi.org/10.1016/j.ijrmm.2019.104086>
- Ding CD, Hu DW, Zhou H, Lu JJ, Lv T (2020) Investigations of P-wave velocity, mechanical behavior and thermal properties of anisotropic slate. *Int J Rock Mech Min Sci* 127:104176. <https://doi.org/10.1016/j.ijrmm.2019.104176>
- Fuenkajorn K, Phueakphum D (2010) Effects of cyclic loading on mechanical properties of Maha Sarakham salt. *Eng Geol* 112:43–52. <https://doi.org/10.1016/j.enggeo.2010.01.002>
- Gu HL, Tao M, Li XB, Momeni A, Cao WZ (2019) The effects of water content and external incident energy on coal dynamic behaviour. *Int J Rock Mech Min Sci* 123:104088. <https://doi.org/10.1016/j.ijrmm.2019.104088>
- Hamza O, Stace R (2018) Creep properties of intact and fractured muddy siltstone. *Int J Rock Mech Min Sci* 106:109–116. <https://doi.org/10.1016/j.ijrmm.2018.03.006>
- Heap MJ, Baud P, Meredith PG, Bell AF, Main IG (2009) Time-dependent brittle creep in Darley Dale sandstone. *J Geophys Res Solid Earth*. <https://doi.org/10.1029/2008JB006212>
- Hou RB, Zhang K, Tao J, Xue XR, Chen YL (2019) A nonlinear creep damage coupled model for rock considering the effect of initial damage. *Rock Mech Rock Eng* 52:1275–1285. <https://doi.org/10.1007/s00603-018-1626-7>



- Jaeger JC, Cook NGW, Zimmerman RW (2007) Fundamentals of rock mechanics, 4th edn. Blackwell Publishing Ltd, Oxford
- Jia CJ, Xu WY, Wang RB, Wang SS, Lin ZN (2018) Experimental investigation on shear creep properties of undisturbed rock discontinuity in Baihetan Hydropower Station. *Int J Rock Mech Min Sci* 104:27–33. <https://doi.org/10.1016/j.ijrmms.2018.02.011>
- Jiang CB, Duan MK, Yin GZ, Wang JG, Lu TY, Xu J, Zhang DM, Huang G (2017) Experimental study on seepage properties, AE characteristics and energy dissipation of coal under tiered cyclic loading. *Eng Geol* 221:114–123. <https://doi.org/10.1016/j.engge.2017.03.005>
- Jiang YJ, Wang YH, Yan P, Luan HJ, Chen YQ (2019) Experimental investigation on the shear properties of heterogeneous discontinuities. *Geotech Geol Eng* 37:4959–4968. <https://doi.org/10.1007/s10706-019-00955-5>
- Kong XG, Wang EY, He XQ, Zhao EL, Zhao C (2019) Mechanical characteristics and dynamic damage evolution mechanism of coal samples in compressive loading experiments. *Eng Fract Mech* 210:160–169. <https://doi.org/10.1016/j.engfracmech.2018.04.005>
- Li CB, Gao C, Xie HP, Li N (2020) Experimental investigation of anisotropic fatigue characteristics of shale under uniaxial cyclic loading. *Int J Rock Mech Min Sci* 130:104314. <https://doi.org/10.1016/j.ijrmms.2020.104314>
- Li QC, Wang HP, Yuan L, Wang W, Hou WT, Ma ZW, Zhang QY (2019) Experimental study of damage and degradation of coal by adsorbed gas amount. *J China Univ Min Technol* 48:955–965. <https://doi.org/10.3321/j.issn:1000-6915.2009.05.002>
- Li ZL, Dou LM, Cai W, Wang GF, Ding YL, Kong Y (2016) Roadway stagger layout for effective control of gob-side rock bursts in the longwall mining of a thick coal seam. *Rock Mech Rock Eng* 49:621–629. <https://doi.org/10.1007/s00603-015-0746-6>
- Ma LJ, Liu XY, Fang Q, Xu HF, Xia HM, Li EB, Yang SG, Li WP (2013) A new elasto-viscoplastic damage model combined with the generalized Hoek-Brown failure criterion for bedded rock salt and its application. *Rock Mech Rock Eng* 46:53–66. <https://doi.org/10.1007/s00603-012-0256-8>
- Ma XD, Haimson BC (2016) Failure characteristics of two porous sandstones subjected to true triaxial stresses. *J Geophys Res Solid Earth* 121:6477–6498. <https://doi.org/10.1002/2016JB012979>
- Mansouri H, Ajallooeian R (2018) Mechanical behavior of salt rock under uniaxial compression and creep tests. *Int J Rock Mech Min Sci* 110:19–27. <https://doi.org/10.1016/j.ijrmms.2018.07.006>
- Masoudian MS, Airey DW, El-zein A (2014) Experimental investigations on the effect of CO<sub>2</sub> on mechanics of coal. *Int J Coal Geol* 128–129:12–23. <https://doi.org/10.1016/j.coal.2014.04.001>
- Mcbeck J, Ben-zion Y, Renard F (2020) The mixology of precursory strain partitioning approaching brittle failure in rocks. *Geophys J Int* 221:1856–1872. <https://doi.org/10.1093/gji/ggaa121>
- Nicolas A, Fortin J, Regnet JB, Verberne BA, Plümpner O, Dimanov A, Spiers CJ, Guéguen Y (2017) Brittle and semibrittle creep of Tavel limestone deformed at room temperature. *J Geophys Res Solid Earth* 122:4436–4459. <https://doi.org/10.1002/2016JB013557>
- Pan XH, Lü Q (2018) A quantitative strain energy indicator for predicting the failure of laboratory-scale rock samples: application to shale rock. *Rock Mech Rock Eng* 51:2689–2707. <https://doi.org/10.1007/s00603-018-1480-7>
- Pepe G, Mineo S, Pappalardo G, Cevasco A (2018) Relation between crack initiation-damage stress thresholds and failure strength of intact rock. *Bull Eng Geol Environ* 77:709–724. <https://doi.org/10.1007/s10064-017-1172-7>
- Rassouli FS, Zoback MD (2018) Comparison of short-term and long-term creep experiments in shales and carbonates from unconventional gas reservoirs. *Rock Mech Rock Eng* 51:1995–2014. <https://doi.org/10.1007/s00603-018-1444-y>
- Renani HR, Martin CD (2020) Slope stability analysis using equivalent Mohr–Coulomb and Hoek–Brown criteria. *Rock Mech Rock Eng* 53:13–21. <https://doi.org/10.1007/s00603-019-01889-3>
- Shen XD, Arson C, Ding JH, Chester FM, Chester JS (2020) Mechanisms of anisotropy in salt rock upon microcrack propagation. *Rock Mech Rock Eng* 53:3185–3205. <https://doi.org/10.1007/s00603-020-02096-1>
- Si XF, Gong FQ, Li XB, Wang SY, Luo S (2019) Dynamic Mohr–Coulomb and Hoek–Brown strength criteria of sandstone at high strain rates. *Int J Rock Mech Min Sci* 115:48–59. <https://doi.org/10.1016/j.ijrmms.2018.12.013>
- Sone H, Zoback MD (2013) Mechanical properties of shale-gas reservoir rocks—part 2: Ductile creep, brittle strength, and their relation to the elastic modulus. *Geophysics* 78:393–402. <https://doi.org/10.1190/geo2013-0051.1>
- Sun YT, Li GC, Zhang JF, Qian DY (2019) Stability control for the rheological roadway by a novel high-efficiency jet grouting technique in deep underground coal mines. *Sustain* 11:6494. <https://doi.org/10.3390/su11226494>
- Tu QY, Cheng YP, Ren T, Wang ZY, Lin J, Lei Y (2019) Role of tectonic coal in coal and gas outburst behavior during coal mining. *Rock Mech Rock Eng* 52:4619–4635. <https://doi.org/10.1007/s00603-019-01846-0>
- Viète D, Ranjith P (2006) The effect of CO<sub>2</sub> on the geomechanical and permeability behaviour of brown coal: implications for coal seam CO<sub>2</sub> sequestration. *Int J Coal Geol* 66:204–216. <https://doi.org/10.1016/j.coal.2005.09.002>
- Wang DK, Lv RH, Wei JP, Fu QC, Wang YT, Zhang P, Yu C, Yao BH (2019) An experimental study of seepage properties of gas-saturated coal under different loading conditions. *Energy Sci Eng* 7:799–808. <https://doi.org/10.1002/ese3.309>
- Wang YT, Zhou XP, Xu X (2016) Numerical simulation of propagation and coalescence of flaws in rock materials under compressive loads using the extended non-ordinary state-based peridynamics. *Eng Fract Mech* 163:248–273. <https://doi.org/10.1016/j.engfracmech.2016.06.013>
- Wawersik WR, Fairhurst C (1970) A study of brittle rock fracture in laboratory compression experiments. *Int J Rock Mech Min Sci* 7:561–575. [https://doi.org/10.1016/0148-9062\(70\)90007-0](https://doi.org/10.1016/0148-9062(70)90007-0)
- Xie GX, Yin ZQ, Wang L, Hu ZX, Zhu CQ (2017) Effects of gas pressure on the failure characteristics of coal. *Rock Mech Rock Eng* 50:1711–1723. <https://doi.org/10.1007/s00603-017-1194-2>
- Xu G, Huang JX, Hu GZ, Yang N, Zhu JQ, Chang P (2020) Experimental study on effective microwave heating/fracturing of coal with various dielectric property and water saturation. *Fuel Process Technol* 202:106378. <https://doi.org/10.1016/j.fuproc.2020.106378>
- Yang SQ, Jing HW, Wang SY (2012) Experimental investigation on the strength, deformability, failure behavior and acoustic emission locations of red sandstone under triaxial compression. *Rock Mech Rock Eng* 45:583–606. <https://doi.org/10.1007/s00603-011-0208-8>
- Yang SQ, Xu P, Ranjith PG (2015) Damage model of coal under creep and triaxial compression. *Int J Rock Mech Min Sci* 80:337–345. <https://doi.org/10.1016/j.ijrmms.2015.10.006>
- Yang SQ, Yin PF, Ranjith PG (2020a) Experimental study on mechanical behavior and brittleness characteristics of longmaxi formation shale in Changning, Sichuan basin, China. *Rock Mech Rock Eng* 53:2461–2483. <https://doi.org/10.1007/s00603-020-02057-8>
- Yang XH, Ren T, Tan LH (2020b) Estimation of average ejection velocity generated by rib burst under compression load. *Int J Rock Mech Min Sci* 128:104277. <https://doi.org/10.1016/j.ijrmms.2020.104277>
- Yin GZ, Jiang CB, Wang JG, Xu J (2015) Geomechanical and flow properties of coal from loading axial stress and unloading

- confining pressure tests. *Int J Rock Mech Min Sci* 76:155–161. <https://doi.org/10.1016/j.ijrmmms.2015.03.019>
- Zhan QJ, Zheng XG, Du JP, Xiao T (2020) Coupling instability mechanism and joint control technology of soft-rock roadway with a buried depth of 1336 m. *Rock Mech Rock Eng* 53:2233–2248. <https://doi.org/10.1007/s00603-019-02027-9>
- Zhang L, Li XC, Gao JX, An ZX, Yang XH, Nie BS (2019a) Creep characteristics and constitutive model of coal under triaxial stress and gas pressure. *Energy Sci. Eng.* 8:501–514. <https://doi.org/10.1002/ese3.532>
- Zhang ZP, Xie HP, Zhang R, Zhang ZT, Gao MZ, Jia ZQ, Xie J (2019b) Deformation damage and energy evolution characteristics of coal at different depths. *Rock Mech Rock Eng* 52:1491–1503. <https://doi.org/10.1007/s00603-018-1555-5>
- Zhao J (2000) Applicability of Mohr–Coulomb and Hoek–Brown strength criteria to the dynamic strength of brittle rock. *Int J Rock Mech Min Sci* 37:1115–1121. [https://doi.org/10.1016/S1365-1609\(00\)00049-6](https://doi.org/10.1016/S1365-1609(00)00049-6)
- Zhao J, Feng XT, Zhang XW, Zhang Y, Zhou YY, Yang CX (2018) Brittle–ductile transition and failure mechanism of Jinping marble under true triaxial compression. *Eng Geol* 232:160–170. <https://doi.org/10.1016/j.enggeo.2017.11.008>
- Zhou H, Chen J, Lu J, Jiang Y, Meng F (2018) A new rock brittleness evaluation index based on the internal friction angle and Class I stress–strain curve. *Rock Mech Rock Eng* 51:2309–2316. <https://doi.org/10.1007/s00603-018-1487-0>
- Zhou ZL, Tan LH, Cao WZ, Zhou ZY, Cai X (2017) Fracture evolution and failure behaviour of marble specimens containing rectangular cavities under uniaxial loading. *Eng Fract Mech* 184:183–201. <https://doi.org/10.1016/j.engfracmech.2017.08.029>

**Publisher's Note** Springer Nature remains neutral with regard to jurisdictional claims in published maps and institutional affiliations.